Deep learning techniques applied to super-resolution chemistry transport modeling for operational uses

Bertrand Bessagnet, Maxime Beauchamp, Laurent Menut, Ronan Fablet, E Pisoni, P Thunis

Deep Learning Techniques applied to Chemistry Transport Modeling for operational uses

B. Bessagnet[1,2]† and M. Beauchamp[3]†, L. Menut[1], R. Fablet[3], E. Pisoni[2], P. Thunis[2]

[1] LMD/IPSL, École Polytechnique, Institut Polytechnique de Paris, ENS, PSL Université, Sorbonne Université, CNRS, 91128 Palaiseau, France
[2] European Commission, Joint Research Centre (JRC), Ispra, Italy
[3] IMT Atlantique, Lab-STICC UMR CNRS, 655 Avenue du Technopôle, 29280 Plouzané, France

E-mail: bertrand.bessagnet@lmd.ipsl.fr, bertrand.bessagnet@ec.europa.eu

Abstract. Air quality modeling tools are largely used to assess air pollution mitigation and monitoring strategies. While neural networks (NN) were mostly developed based on observations to derive statistical models at stations, the use of Eulerian chemistry transport models (CTMs) was mainly devoted to air quality predictions and the evaluation of emission reduction strategies. In this study, we investigate deep learning architectures to create a surrogate model of the CTM CHIMERE and significantly reduce the computing times required for high resolution simulations. The key point is the selection of input variables and the way to implement them in the NN. We perform a quantitative evaluation of the proposed approaches on a real case-study. The best NN architecture displays very good performances in terms of prediction of pollutant concentrations observed at stations w.r.t. high-resolution CHIMERE groundtruth, with a correlation coefficient above 0.95. The best NN is also able to display better performances when compared to observations than the raw high resolution simulation.

Keywords: Air Pollution, Deep Learning, Modeling, Multi-Layer Perceptron, Convolutional Neural Network

† co-first authors

1. Introduction

Nowadays, around 55% of the world's population lives in urban areas, and this number is expected to increase by 68% by 2050 [1]. AS stated in the European Environment Agency annual report, around 25% of the European urban population is exposed to air quality exceeding the European Union air quality standards, and air pollution is the leading preventable risk factors for premature death in Europe, being responsible for 400,000 deaths per year directly or indirectly [2]. The simulation of Air Quality in urban areas remains a major challenge, in particular to assess the exposure of citizens to pollutants, identify the sources of pollution and adapt the strategies to improve the situation. Operational models are expected to be more robust and computationally-efficient to quickly simulate air quality and propose adequate measures to monitor, curb and control air pollution. On the regional scale, operational forecasting system mainly rely on deterministic models that perform simulations with average resolutions of 10km in the case of a European domain and 3km to 1km for a regional domain. A chemistry transport model like CHIMERE [3] is suitable to work at such resolutions. This type of models is used in well-known platforms such as the COPERNICUS ensemble forecast [4], the French national forecast PREV'AIR [5], the regional forecasts of air quality monitoring associations in France Airparif [6].

Machine learning techniques have also emerged as relevant solutions to forecast air quality at stations and using observations (meteorology, concentrations, emissions, landcover, etc.) as predictor variables [7, 8, 9, 10, 11, 12, 13]. Recently, deep learning schemes based on neural networks (NN) [14] has become more and more popular with increasing computer power and training data availability. They seem now relevant and possible to use in the air quality community. These studies show the need to evaluate: (i) the influence of the length of training data utilized on the overall NN model performance,(ii) the significance of the selected predictors and utilized model structure on the complexity and overall NN model performance, (iii) the links between the selected data normalization scheme and transfer function utilized and (iv) the influence of the adapted initialization schemes for the weighting, bias and other training parameters on the overall NN model performance.

Some very recent works propose to embed NN techniques with CTM models, the objective being to get the best of state-of-the-art physics on-board CTMs and NN approaches [15, 16]. For instance, in [15], neural network schemes were tested to emulate process-oriented modeling outcomes. Especially, they esigned a simple recurrent 3-layer NN to reproduce daily mean concentrations of some pollutants over Europe as simulated by the Community Multiscale Air Quality model (CMAQ). The trained NN may estimate air pollutant concentrations several orders faster than the original model and with reasonably small errors. They designed a simple recurrent 3-layer NN to reproduce daily mean concentrations of some pollutants over Europe as simulated by the Community Multiscale Air Quality model (CMAQ).

Following these previous works, this study proposes a novel approach to design a

NN-based emulator of high-resolution air pollution simulations [17], which are highly time-consuming. In [17], we showed that a very simple regression with an adequate selection of input variables may relevantly emulate a CTM and mimic the behavior with identical performances. Though, this preliminary study was made on daily datasets and complementary developments still have to be made on hourly datasets and domains with intricate downscaling from coarse to high resolution. Here, we introduce a new CTM-NN strategy. Compared with previous works, the novelty of our approach lies in the input data selection and the designed NN architectures. We report a quantitative evaluation on a representative test case, which demonstrates the relevance of the proposed CTM-NN approach. We further discuss possible applications and improvement for operational uses.

2. Methods

2.1. The original principles

In a previous study [17], a surrogate model of the CTM CHIMERE was designed to downscale a low 0.50.25 horizontal resolution simulation to a higher 0.093750.046875 resolution. The use of air quality models is highly computionnally-demanding mainly because of the CourantFriedrichsLewy (CFL) condition. The CFL condition is a necessary condition for convergence when partial differential equations are numerically solved by finite differencing. This condition imposes to adopt an adaptive time step. For the advection, the time step is proportional to the grid size for the horizontal transport involving in some cases a dramatic increase of the span of simulation.

The first version of this methodology was based on a training process over a 6-months period and applied over the subsequent 6 months with an evaluation against the performances and results of the raw CHIMERE simulation at high resolution. This simple methodology provided means to assess the extent to which the proposed approach capture the main patterns and evolution of daily concentrations for the main pollutants, and the gain in computing time was very important since the costly step of the simulation process is by-passed. Performances based on an evaluation against observations were similar to those obtained with the raw model simulations with CHIMERE at high resolution. In the following uppercase letter refer to variables at low/coarse resolution (LR) and lowercase for the high resolution simulation (HR), the bases of the methodology is described hereafter.

In [18, 17], a given high resolution grid cell was assumed to behave as a "city". Based on atmospheric diffusion theory, potential determinants of urban increments and functional forms of their relationships have been hypothesized [19] as follows. Thus, under neutral atmospheric conditions, the vertical diffusion of a non-reactive pollutant from a continuous point source can be described in general form through the following relationship assuming a Gaussian dispersion in a box model approach:

$$\sigma_z^2 = \frac{2kx}{u} \tag{1}$$

with σ_z^2 indicating the variance of the vertical diffusion after a distance x from the source, k as the eddy diffusivity and u as the wind speed.

As described in [18, 17], a generalization of this equation has been hypothetized to evaluate the concentration difference Δc between a fine grid and a coarse grid simulation of a primary pollutant p concentration influenced by low level sources of primary pollutants which can be finally expressed as:

$$c = C + \Delta c \tag{2}$$

$$\Delta c = \alpha \frac{1}{\sqrt{ku}} \left(e\sqrt{d} - E\sqrt{D} \right) + \beta \tag{3}$$

$$d \propto \sqrt{\delta x \delta y} \tag{4}$$

$$D \propto \sqrt{\delta X \delta Y} \tag{5}$$

- c and C (μg m^{-3}) are respectively the concentrations at the high resolution (HR) and the low resolution (LR) interpolated from the coarse grid to the fine mesh, k is the vertical mixing coefficient (m^2 s^{-1}) at the fine grid, u is the 10m horizontal wind speed (m s^{-1}) at the fine grid, δX, δY, δx, δy are respectively the coarse longitude, latitude and the fine longitude, latitude increments of the grids (in degree). In our study they are constant, but they can vary and for each fine grid cell an average value of the surrounding coarse grids can be used.
- d and D are characteristic lengths respectively for the fine and coarse meshes, they correspond here to an average of the grid cells size.
- e and E (μg m^{-2} s^{-1}) are respectively high resolution and coarse resolution low-level emission fluxes at the fine grid point. E is interpolated from the coarse grid. For the $PM_{2.5}$ and PM_{10} concentrations, the sum of the primary emissions is considered while for NO and NO_2 the NOx emissions are considered. In the methodology, the emissions of the two first level (sum of emissions approximately below 30 m) of CHIMERE are taken into account.
- α and β are regression coefficients embedding geographical, physical and chemical processes for which details are lost during the simplification process, they also account for unit changes. Note that β here has not the same meaning than in [18, 19], it represents here the residual value of the regression method and would be expected to be close to 0.

An illustration of this concept is displayed in Figure 1. As explained in the next sections, the previous equations list the relevant variables which are selected as inputs for the NN.

2.2. CHIMERE ouputs as input for the Neural Networks

The CHIMERE configuration used to create the input data for our neural network strategies is summarized here, but the reader can refer to the reference CHIMERE

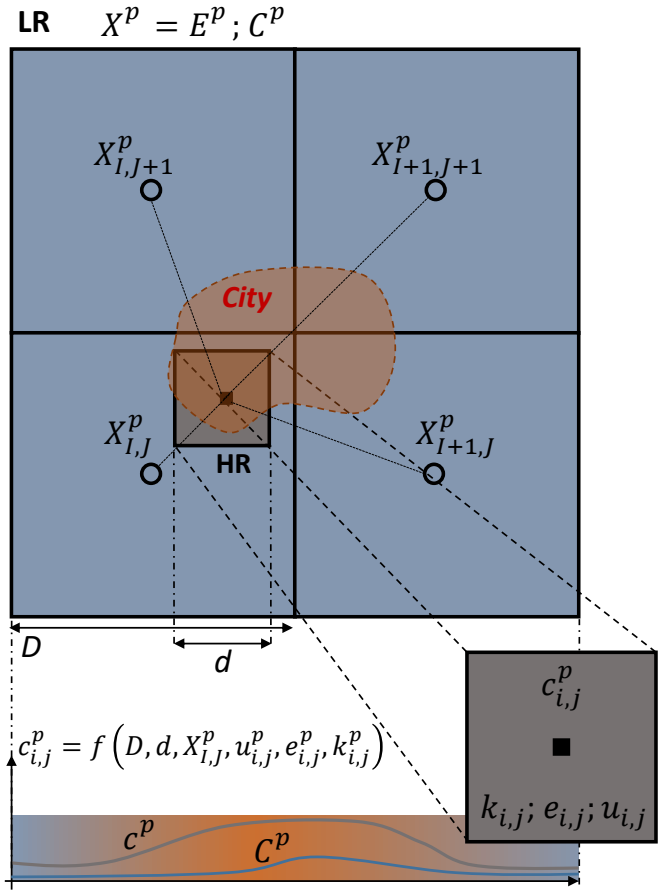

Figure 1: Illustration of the relation between high and low resolutions of all variables with the Δ concept. The presence of a city is responsible of an increase Δc of primary pollutant concentrations enhanced by local meteorology and emissions. The coarse resolution variables C and E as used in input for the NN are reinterpolated over the fine mesh APL0033 here.

publications [3, 20, 21, 22] for details on the corresponding model components and references as well as non user-specific model characteristics. The gas-phase chemical mechanism is MELCHIOR2, which consists of a simplified version (more than 40 species and 120 reactions) of the full chemical mechanism based on the concept of chemical operators. Modeled particulate matter includes primary particulate matter, and secondary inorganic (nitrate, sulfate, ammonium based on the ISORROPIA thermodynamic equilibrium model) and organic aerosol resulting from the oxidation of the relevant anthropogenic and biogenic precursors and gas-particle partitioning of the condensable oxidation products [22]. Biogenic emissions are computed with MEGAN version 2.1 [23], sea-salt and mineral dust emissions from desert and agricultural areas are also considered. Particle sizes range from 10nm to 40μm over 10 bins. SIA, SOA, OM, EC, DUST, SALT, PPM respectively referred as Secondary Inorganic Aerosol (sum of nitrate, sulfate and ammonium), Secondary Organic Aerosols (anthropogenic and biogenic in origins), Organic Matter, Elemental Carbon, natural mineral dust,

sea salt and Primary Particle Matter (primary anthropogenic carbonaceous and non-carbonaceous species) are considered for the PM composition. For the meteorology, the WRF 3.7.1 version is used. The WRF simulation has been nudged with NCEP (National Centers for Environmental Prediction) final analysis meteorological fields GFS (Global Forecast System) at 1x1^o and 6-hourly time resolution at the coarsest model initial and domain boundaries (ds083.2 dataset, [24]).

Table 1: Domain specifications (BOUN: Boundary conditions, INIT: Initialization)

Domain Name	**EUR01**	**ALP0033**
Area	Western Europe	French Alps
Coverage	11.85^{o}W-33.25^{o}N/33.85^{o}E-60.85^{o}N	4.417^{o}E-44.317^{o}N/7.783^{o}E-46.583^{o}N
Number of grid points	459 × 278	103 × 70
Resolution	$1/10^o \times 1/10^o$	$1/30^o \times 1/30^o$
Number of CHIMERE levels	15	20
Chemical BOUN-INIT	LMDzINCA GOCART	EUR01
Met. BOUN-INIT	NCEP/GFS	EUR01
Met. Nudging	Yes	No

For this study, the set-up and domains are rigorously the same depicted in a previous work aiming at simulating the air quality at fine resolution over the French Alps [25] providing CTM outputs for the meteorology and concentrations fields. Two different domains are defined as: (i) EUR01 covering a large part of Western Europe and (ii) over ALP0033 for the whole French Alps with detailed characteristics are detailed in Table 1. The Alps domain (APL0033) encompasses an area from the Lyon municipality on the West part to the Leman Lake on the north to the Piemonte region in Italy on the East Part with a resolution of about 3km (Figure 2). Grenoble and the Arve valley from Geneva to Chamonix are known to be air pollution hot spots in France due to their location in deep valleys with frequent stagnant cold meteorological conditions in wintertime. The HR simulation is performed over the ALP0033 and the LR simulation over the EUR01 domain and interpolated over the ALP0033 so that the ALP0033 mesh will be the working grid for the neural networks. The simulation was performed from 2013-11-15 01:00 UTC to the 2021-12-21 00:00 UTC with a spin-up period from the begin of November to ensure a good initialization. Therefore 864 hours are available to train (432 hours) and evaluate (432 hours) the various neural network strategies. The available observation dataset for model evaluation is reported in [25] with rural and urban background stations (Figure 2).

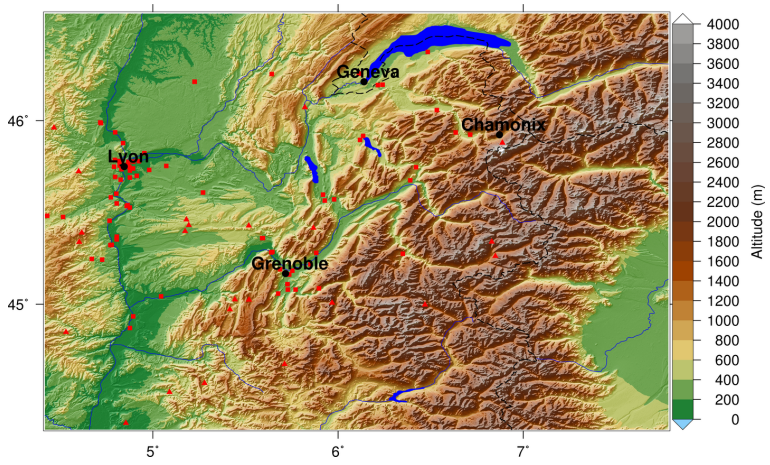

Figure 2: The target domain over the Alps (ALP0033). Red triangle and square symbols are respectively the locations of rural and urban air quality monitoring sites used for the evaluation. Dark blue color is used for water bodies.

2.3. NN-based architecture in this study

The basic concept of our approach is presented in Figure 3. We aim to replace the high resolution simulation HR by a neural-network-based model to save computing time so that we could produce quick scenarios analyses or air quality predictions. The key idea is to exploit the low resolution in the inputs of the NN to convey an information on chemistry and long range transport processes that are of major importance for air pollution issues.

In [17], the downscaling from coarse/low (LR) to high (HR) resolution is performed by N pixel-grid linear regressions of the increment Δc based on Eq.3, where N denotes the number of grid cells in the HR target ALP0033. In this work, we consider an extension of this preliminary work with more sophisticated deep learning-based models. We aim to train as N location-specific independent super-resolution (SR) operators $\Phi = \{\Phi_i\}, i = 1, \cdots, N$ where $c_i^\star = \Phi_i(C_i, \Lambda_i)$, $c_i^\star$ and C_i respectively denote the estimation of the high and coarse resolution (this latter been interpolated over the fine mesh ALP0033) in grid cell/pixel i, and $\Lambda_i = (d, D, e, E, k, u)_i$ denotes as used in Eq.3 the set of additional covariates at the same location over the high resolution mesh ALP0033. The first natural generalization of [17] is to involve independent pixel-grid multi-layer perceptron (MLP) for SR operator Φ, see Figure 4, instead of a linear regression. Here, we use a MLP architecture with two hidden layers of 16 and 8 neurons with ReLU (Rectified Linear Unit) activation and a final linear mapping to $c_i^\star$. Instead of constraining the inputs of the network to variable $\frac{1}{\sqrt{ku}}\left(e\sqrt{d} - E\sqrt{D}\right)$ used in the linear regression, we simply feed the MLP with all the potential covariates, namely C, k, u, d, D, e and E and let the training extract the relevant features through the weight parameters of the first two hidden layes of the MLP. This choice provides more flexibility. In this configuration, the number of parameters for each submodels Φ_i is 289. In the

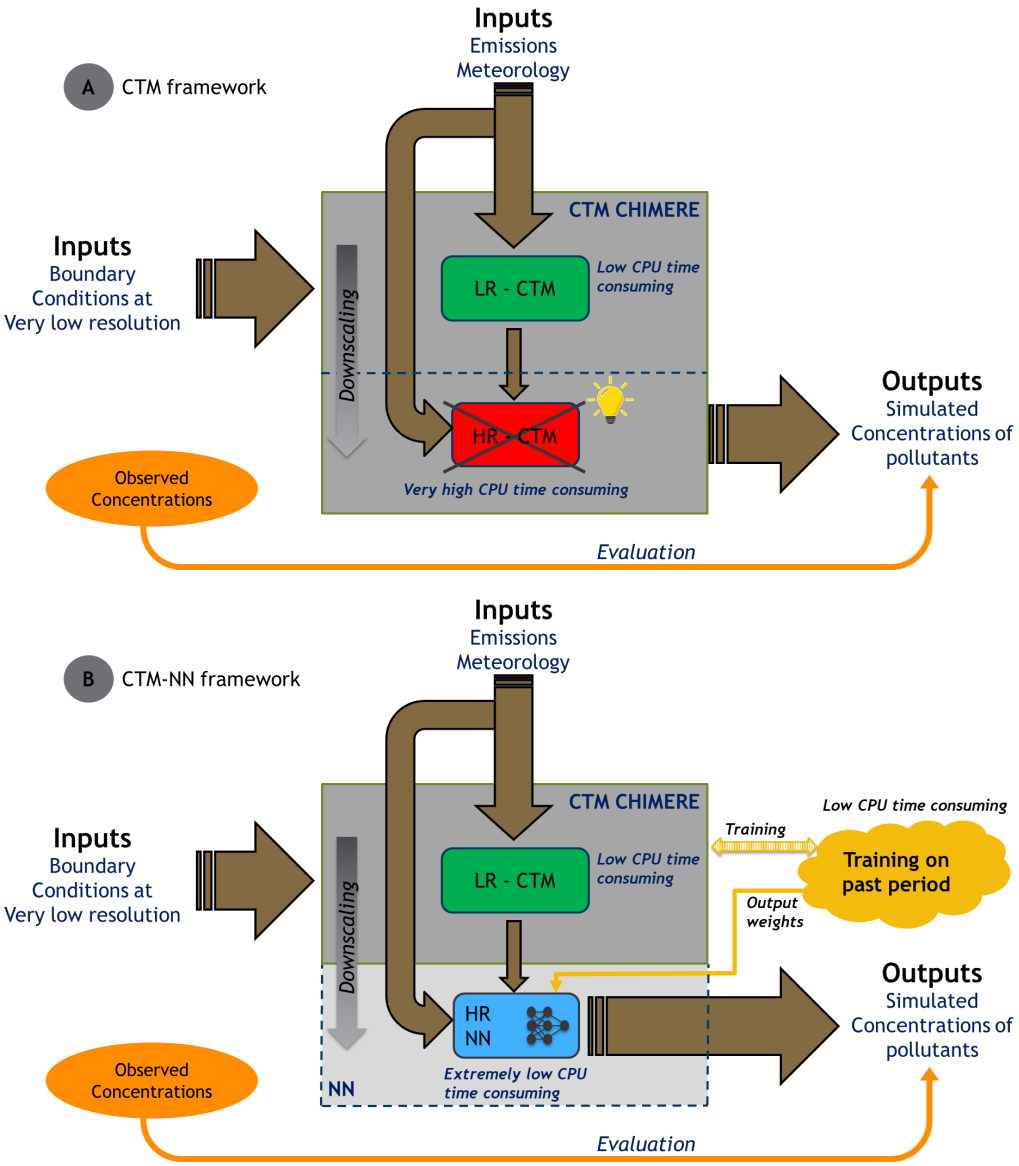

Figure 3: Conceptual scheme of the methodology. Panel (A) at the top is the presentation of the usual concept of air quality model with two domains at low and high resolutions (LR and HR respectively). Panel (B) is the new concept using a NN to skip the most time consuming HR-CTM simulation

end, on the global 69x102 ALP0033 domain, the total number of parameters is 2033982. The test case here differs from [17] where a 12 months period was used for the training and validation and only the daily values where exploited. In this new study a shorter period of 36 days is used and the training and validation processes are performed on an hourly basis.

Because the working frame is a two-dimensional fields discretized on a regular grid, additional options may be envisaged for SR operator Φ by considering the use

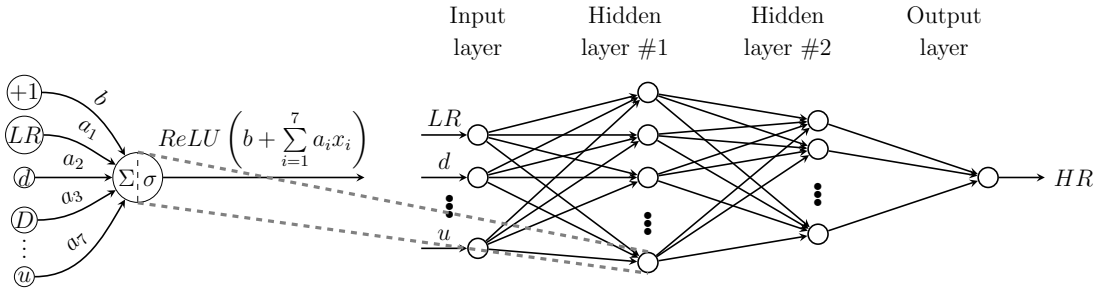

Figure 4: Pixel-independent Multi Layer Perceptron (MLP)

of convolutional neural networks (CNN) [14]. The underlying idea is to exploit the potential spatial relationships within local neighborhoods to ease the learning of Φ which will be a global SR operator and not an aggregation of N independent pixel-grid SR operators. This framework can be extended to spatio-temporal CNN even though we believe that for this super-resolution task, a spatial formulation of the problem is satisfactory enough. This is still an interesting idea though if the same work has to be achieved on data with high missing data rates, such as remote sensing and/or in-situ dataset [26]. Here, a simple CNN architecture is first considered in which the inputs are the same covariates used in the MLP, but stacked here in addition of the coarse resolution C as supplementary channels. The CNN architecture comprises a first hidden layer with 128 Conv2D 3x3 filters + ReLU activation (Rectified Linear Unit) with a batch normalization, followed by a second hidden layer with 64 5x5 filters + ReLU activation. The final layer maps the outputs of the second hidden layer to the required HR resolution by a single linear Conv2D 3x3 filter, see Figure 5. The total number of parameters for this CNN is 84737.

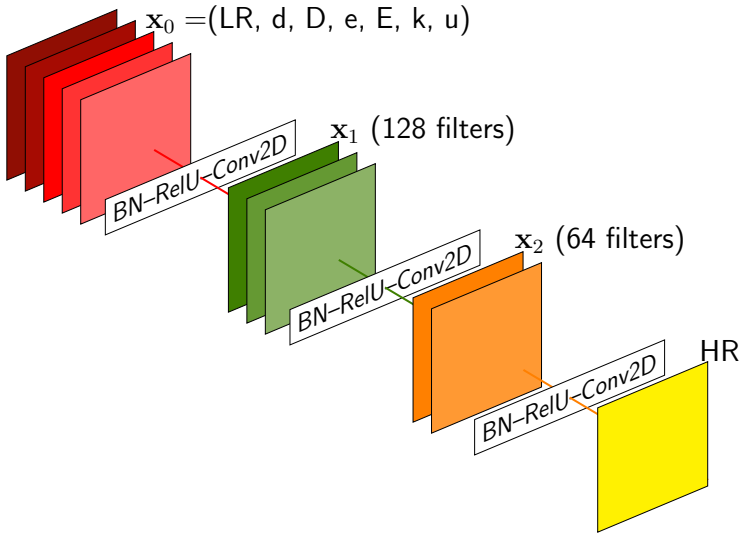

Figure 5: Convolutional Neural Network (CNN) architecture

We also draw from the learning-based super-resolution literature to evaluate more

sophisticated CNN architecture. Here, we consider the Deep Residual Channel Attention Networks (RCAN) architecture [27], which is among the state-of-the-art deep learning models for the super-resolution of natural images. In this setup, the so-called residual-in-residual (RIR) structures are the elementary building blocks of the deep neural network architecture. RIR blocks are typically made up of several residual groups (RG) with long skip connections, while each residual group itself contains a predefined number of residual cells with short skip connections. The underlying idea lies in the fact that RIR blocks allows to bypass low-frequency information through multiple skip connections, thus allowing the main network to focus on the learning of high-frequency information. The RCAN architecture also involves a channel attention-based mechanism [28, 29] to rescale channel-wise features through interdependencies among channels. The total number of parameters in our RCAN configuration is 299,393.

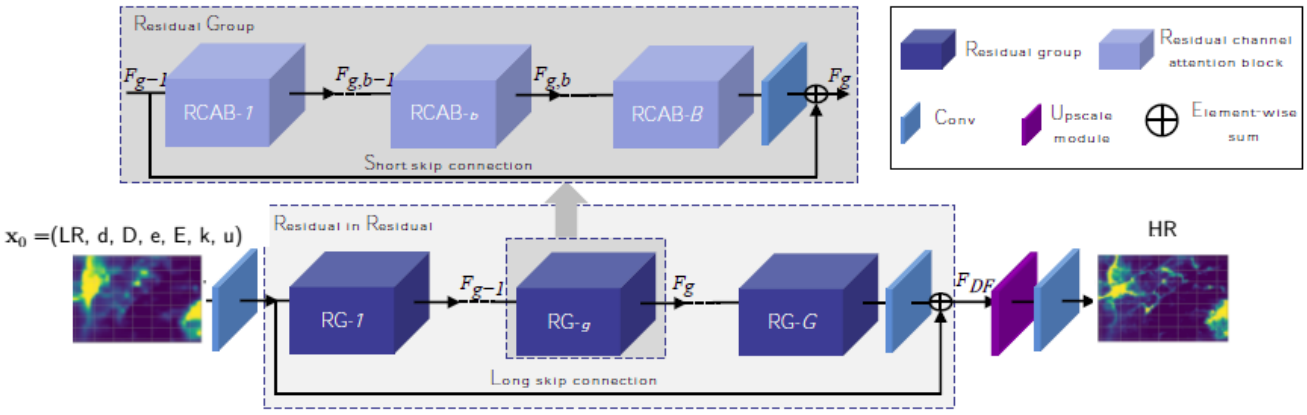

Figure 6: Deep Residual Channel Attention Networks (RCAN) architecture, *picture adapted from [27]*

The so-called back-propagation strategy to calculate the fitting coefficient of the NN is the essence of neural net training. It is the practice of fine-tuning the weights of a neural net based on the error rate (*i.e.* loss) obtained in the previous epoch (*i.e.* iteration). Proper tuning of the weights ensures lower error rates, making the model reliable by increasing its generalization. Regarding the training phase, we use for all architectures as training loss function $\mathcal{L}$ the root mean squared error between the "true" high resolution (c_i) and the output of the neural network ($c_i^\star$):

$$\mathcal{L} = \frac{1}{N}\sum_{i=1}^{N}(c_i^\star - c_i)^2$$

It is noteworthy that it could be interesting in future works to assess if other loss functions can be of interest, for instance to constrain the SR operator Φ to behave better during pollution episodes. Regarding the training strategy, we use an Adam optimizer with a batch size of 4 through 200 epochs on a Microsoft Azure Virtual Machine (VM) powered by NVIDIA Tesla K80 with a GPU memory of 12GiB. The training time of a

single MLP is only of 15 seconds, but without any parallelization, the whole training on the 7038 grid cells of the ALP0033 domain is about 26 hours. The CNN-based architectures provide faster training procedures with only 50 minutes for the basic CNN and around 6 hours for RCAN. In the end, if the training time can significantly differ according to the NN architecture, their application on new datasets only takes a few seconds. All NN models are implemented using keras framework.

3. Results

In this Section, we report the results obtained for NO_2 and $PM_{2.5}$ with the three NN-based super resolution strategies. We use the first half of the dataset for training: 432 hours ranging from 2013-11-15 01:00 UTC to 2013-12-03 00:00 UTC and the other half for validation, ending on 2013-12-21 00:00 UTC. Complementary results are provided in Appendix A for PM_{10} and the evaluation on an hourly basis in Appendix B. Appendix C provides an evaluation on δC for each NN. The definition of evaluation metrics is provided in Appendix D.

Typical patterns of high concentrations are observed along the road traffic network and urbanized areas with the original high resolution (HR). $PM_{2.5}$ concentrations maps are smoother since PM emissions are more spread over rural areas particularly due to wood burning and long range transport of such species. Figure 7a and 7b respectively show the NO_2 and $PM_{2.5}$ mean concentrations over the validation period. CHIMERE high-resolution (top left panel) is the target that the super resolution NN operator aims at reconstructing, starting from the coarse resolution (top right panel) and additional covariates as input datasets. On the bottom panel, the maps obtained with the three NN-based super resolution architectures are displayed: from left to right MLP, CNN and RCAN. They all exhibit a significant improvement as compared to the coarse simulation. The main patterns are well reproduced by the three NN architectures while the coarse resolution acts like a smoother of both NO_2 and $PM_{2.5}$ pollution level in these areas of interest.

Because the $PM_{2.5}$ increment of concentrations between the high and coarse resolutions is less easily explained by the high resolution emission covariates, the SRNN applied to $PM_{2.5}$ coarse resolution is slightly less efficient in comparison to the results obtained for NO_2. It is especially noticeable in the southeast quarter of the domain where the convolutional-based SRNN NO_2 downscaling is very similar to the high resolution. Meanwhile, it is not straightforward to say if the modifications of the $PM_{2.5}$ coarse resolution proposed by the SRNNs really bring the simulation closer to the high resolution in this area of the ALP0033 domain.

If the gain provided by the super resolution solution presented here is obvious when looking at the maps, we present in Figure 8a and 8b error statistics between the HR simulations and the various neural networks as Normalized Root Mean Square Error as

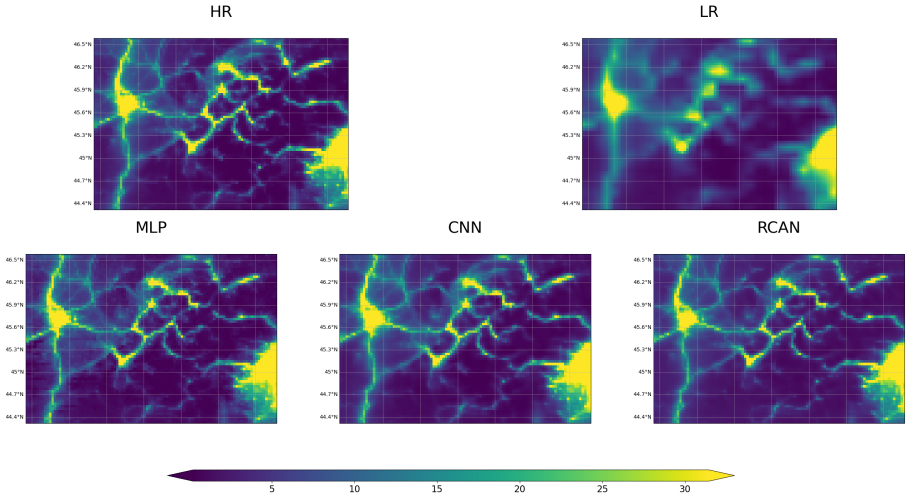

(a) NO_2

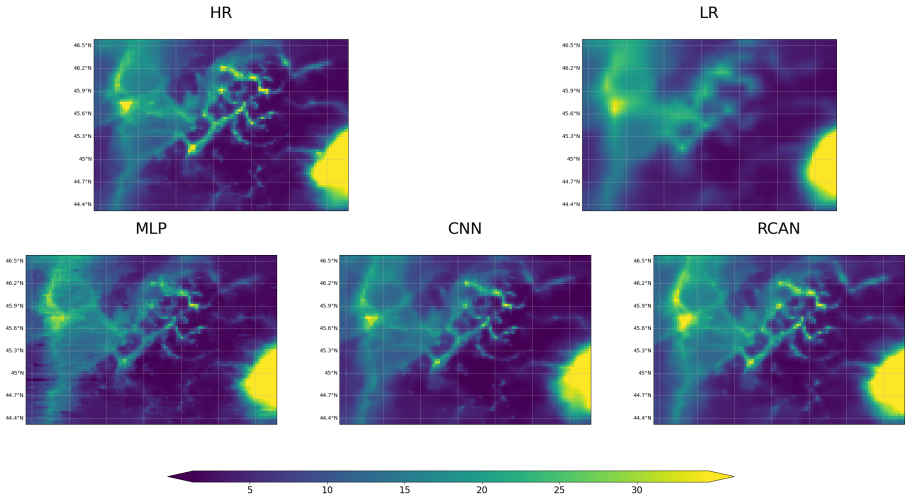

(b) $PM_{2.5}$

Figure 7: NO_2 (a) and $PM_{2.5}$ (b) mean concentrations (μg m^{-3}) over the validation period for CHIMERE high-resolution and coarse resolution (top line) and 3 NN-based super resolution architectures (bottom line): from left to right, pixel-based independent multi-layer perceptron (MLP), Convolutional neural network (CNN) and Residual channel attention network (RCAN)

nRMSE (solid lines) and correlation (dashed lines). These statistics are displayed on an hourly basis in order to identify which NN architecture behaves best along the validation period. Each grid point provide an hourly HR "truth" and SR modeled output. CNN and RCAN architectures seem to increase the already significant gain of the MLP architecture. In terms of correlation, RCAN is slightly better than the basic CNN

architecture but the NO_2 variability of the latter, see the CNN-based standard deviation on the Taylor diagram provided in Figure 9a, is closer to the HR truth. Correlations are usually higher than 0.95 for NO_2 concentrations for the three NN architectures. The hourly frequency results B are similar with again the best performances for the RCAN. It is noteworthy that even the evaluation on Δc for each NN (Appendix C) show the ability of the NN to mimic the Δc of the HR model with a correlation up to 0.95 for NO_2 by the RCAN approach. Regarding the statistics related to $PM_{2.5}$ concentrations, they all indicate RCAN (see Figure 9b) is the best super resolution approach among the three architectures evaluated. On this specific pollutant, it is also interesting to note that RCAN is the single super resolution architecture able to deal with the abrupt change of performance of the coarse resolution in the last hours of December 18 (see Figure 8b): even if the nRMSE and correlation with HR become worse than earlier in the validation period, they are the best trade-off while both the MLP and in a lesser way the CNN do not capture this singularity in the validation period. The same conclusions hold for PM_{10} (see Appendix A). Regarding this specific issue, the $PM_{2.5}$ mapping are also provided in Figure 10 on 2013-12-18 18:00 UTC as complementary information. It is clear that the impact of the emission covariates is here largely overestimated in this situation with low $PM_{2.5}$ pollution levels along the roads. This issue directly relates to the learning issue of optimizing the RMSE loss function in average over this training period. It might be more efficient to consider other loss functions and training datasets to address the issue of learning how the HR behaves in specific conditions for operational applications.

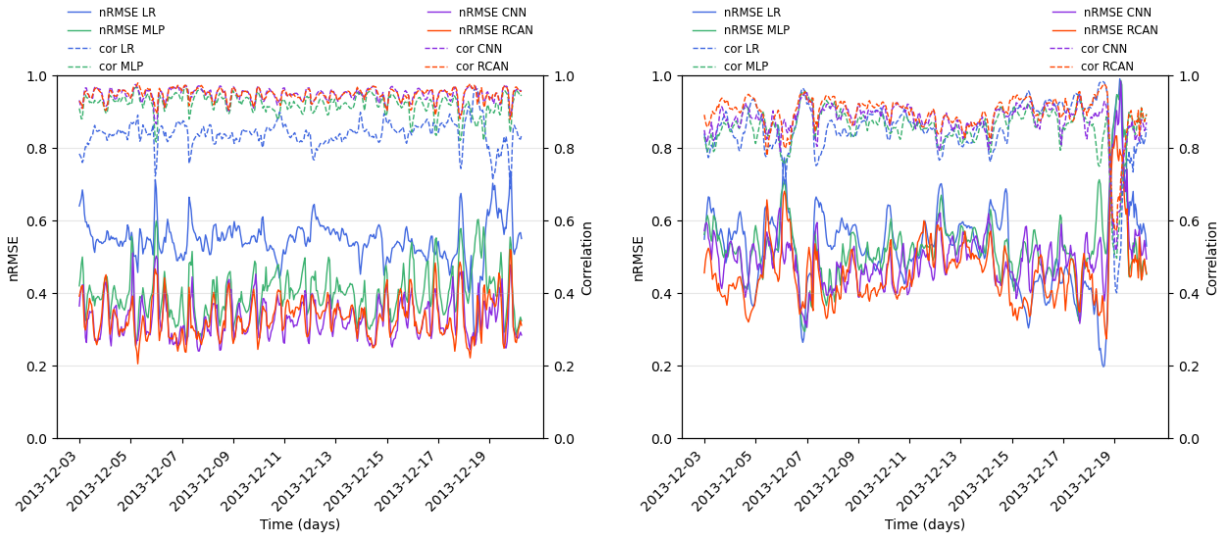

(a) NO_2 (b) $PM_{2.5}$

Figure 8: NO_2 (a) and $PM_{2.5}$ (b) nRMSE and correlation time series (a) of coarse resolution, pixel-based independent multi-layer perceptron (MLP), Convolutional neural network (CNN) and Residual channel attention network (RCAN).

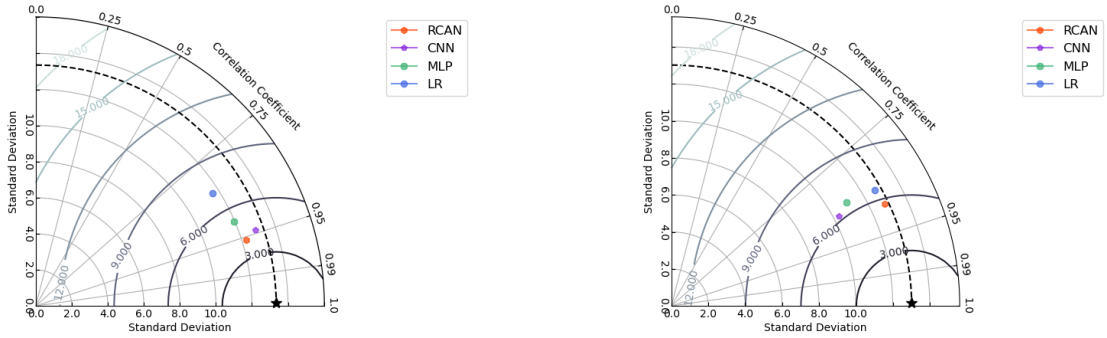

(a) NO_2 (b) $PM_{2.5}$

Figure 9: NO_2 (a) and $PM_{2.5}$ (b) summary statistics over the validation period as Taylor diagrams for low resolution simulation (LR), multi-layer perceptron (MLP), Convolutional neural network (CNN) and Residual channel attention network (RCAN) versus the high resolution (HR) considered as the "truth".

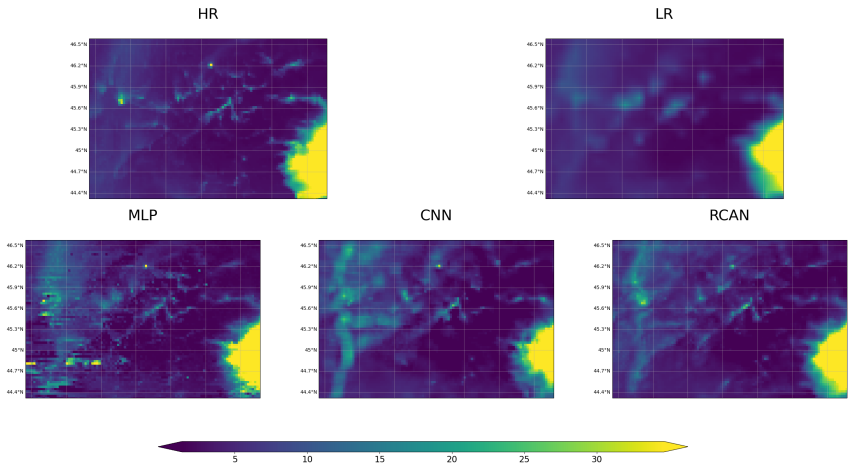

Figure 10: $PM_{2.5}$ concentrations on 2013-12-18 18:00 UTC for CHIMERE high-resolution and coarse resolution (top line) and the three NN-based super resolution architectures (bottom line): from left to right, pixel-based independent multi-layer perceptron (MLP), Convolutional neural network (CNN) and Residual channel attention network (RCAN).

As in [17] it is interesting to compare the HR, LR and the three NN simulation outputs with observation data. For the observations available in the ALP0033 domain along the validation period, we provide in Figures 11 and 12 additional Taylor diagrams for the comparison of HR, LR, and the three SRNN to daily-averaged rural and urban observations. Complementary statistics (average bias, RMSE and correlation) are also given in Tables 11c and 12c, as well as the original hourly statistics in Appendix B: they lead to the same conclusions except that the MLP architecture might improve in terms

of RMSE and correlation at the expense of a degraded variability. Regarding the NO_2, because the high-resolution behaves badly/relatively poorly(?) on the rural observations with an average correlation lower than 0.25, it is not surprising to see the SRNNs doing the same. For urban areas, we report a greater similarity ot the HR groundtruth for all NN models with an average correlation of 0.75 for SR-MLP model and slightly lower performance for SR-CNN and SR-RCAN ones (0.70 for the basic CNN and 0.71 for RCAN). This raises the legitimate issue of data assimilation in CTM high-resolution simulation for which SRNN models open new avenue because they can provide a plug-and-play surrogate models in a classic data assimilation framework [30, 31, 32]. They can also be extended to a fully NN-based data assimilation scheme, where the end-to-end learning strategy consists in using both the coarse resolution (with the HR covariates) and the observations to feed a neural network whose target is the anomaly between the observations and the coarse resolution [33, 26]. Also, these formulations have the advantage of addressing both interpolation, reconstruction and forecasting issues where only a combination of LR and HR covariates, possibly irregularly-sampled, are available.

Performances on $PM_{2.5}$ concentrations for the HR resolution at rural stations is better than for NO_2 with an average correlation of 0.70 and RMSE of 5.62 μg m^{-3}; for this pollutant, the CNN-based architectures are even closer to the observations than HR with an improvement of the correlation up to 0.82 with the basic CNN and a similar RMSE with RCAN. Even at urban sites, RCAN behaves better than HR with similar correlations but lower RMSE and biases. This supports the use of such a super resolution approach as surrogate model in operational applications.

4. Discussion

The best NN architecture RCAN is able to reproduce the behavior of the raw HR simulation with satisfactory performances. For some pollutants the NN model is even able to provide better results probably by smoothing some aberrant values calculated by the CTM during very stable situations leading to unrealistic concentration peaks. With minor improvements on ozone chemistry and the use of observational data to constrain the system similarly to MOS (Model Output Statistic) techniques, our approach can be quickly deployed for air quality forecasting. Once the training is performed the forecasting chain could deliver a forecast in a few second instead of hours. Then, it should be further investigated if a generic NN-based model is sufficient or if it has to be adapted to specific meteorological conditions. In the latter, a training strategy must be investigated with probably a moving 15 days or a monthly update of the learning process taking the last 15 to 30 days for instance. This would have the advantage of training the NN with similar meteorological conditions.

More interesting, expectations lie in the field of air quality modeling for policy making and impact assessment. These NN approaches can be complementary of statistical analysis embedded in surrogate models like the Screening for High Emission

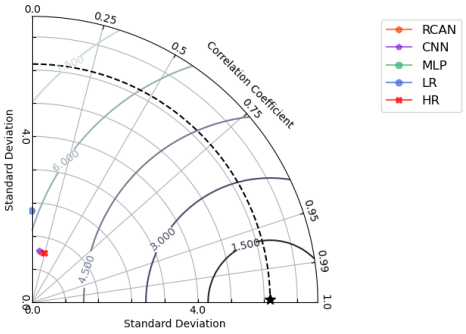

(a) All rural

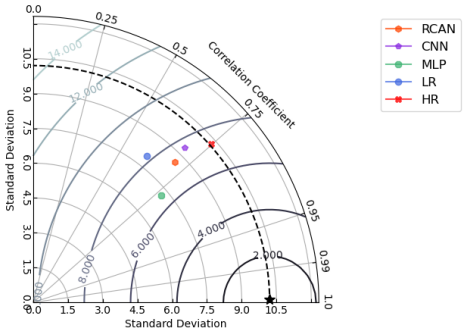

(b) All urban

Species	Method	Typology	# stations	Obs.	Mod.	Bias	RMSE	Cor.
NO_2	HR	RUR	7	13.10	4.73	-8.37	10.06	0.24
	LR				5.54	-7.56	9.76	-0.01
	MLP				4.19	-8.91	10.83	-0.12
	CNN				4.81	-8.29	10.07	0.13
	RCAN				4.58	-8.53	10.23	0.19
	HR	URB	40	47.83	33.37	-14.46	16.19	0.75
	LR				24.45	-23.39	24.79	0.61
	MLP				30.16	-17.67	18.85	0.77
	CNN				31.14	-16.69	18.35	0.70
	RCAN				29.78	-18.05	19.47	0.71

(c) Daily statistics

Figure 11: NO_2 daily statistics of high resolution (HR), coarse resolution (LR), pixel-based independent multi-layer perceptron (MLP), Convolutional neural network (CNN) and Residual channel attention network (RCAN) for comparison with all rural observations (a) and all urban observations (b) as Taylor diagrams summarized in table (c). Observations, model outputs, biases and RMSE are expressed in μg m^{-3}.

Reduction Potential on Air - SHERPA [34, 35] developed to support the design of air quality plans in the context of the EU Air Quality directive [36] by the member states. The approach proposed in SHERPA is based on the cell-per-cell relationships linking the concentration at a grid cell i to the emissions in the surrounding cells. It builds on the concept of Geographically Weighted Regression (GWR) as used in [37]) or local modeling approaches [38], a family of approaches that uses bell-shaped kernel functions to establish weighted, local regressions between input and output variables. SHERPA is designed to evaluate the impact of an emission reduction for a given activity sector and area to a selected location through the mathematical representation of Source Receptor Relationships (SRR). The SHERPA model works so far on yearly and season averaged concentrations. Working over large time-averaged periods smooths the results and limits the impact of non-linearities induced by complex high-frequency phenomena and interactions between chemical species. SHERPA requires a minimum number of

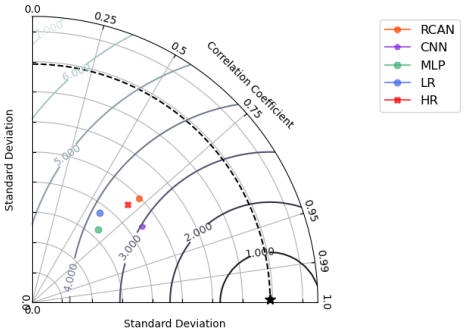

(a) All rural

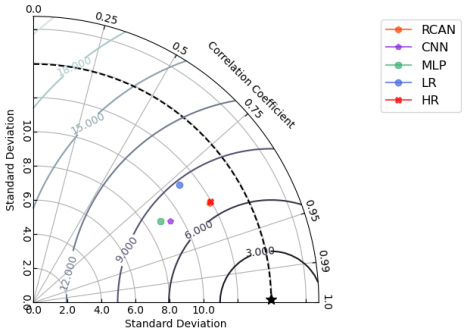

(b) All urban

Species	Method	Typology	# stations	Obs.	Mod.	Bias	RMSE	Cor.
$PM_{2.5}$	HR	RUR	3	12.48	7.85	-4.49	5.62	0.70
	LR				6.30	-6.06	7.15	0.60
	MLP				6.49	-5.89	6.95	0.67
	CNN				6.72	-5.64	6.33	0.82
	RCAN				7.75	-4.58	5.62	0.72
	HR	URB	12	35.68	24.30	-11.36	13.29	0.87
	LR				21.30	-14.37	16.82	0.78
	MLP				21.03	-14.64	16.70	0.84
	CNN				21.34	-14.32	16.21	0.86
	RCAN				25.44	-10.23	12.31	0.87

(c) Daily statistics

Figure 12: $PM_{2.5}$ daily statistics of high resolution (HR), coarse resolution (LR), pixel-based independent multi-layer perceptron (MLP), Convolutional neural network (CNN) and Residual channel attention network (RCAN) for comparison with all rural observations (a) and all urban observations (b) as Taylor diagrams summarized in table (c). Observations, model outputs, biases and RMSE are expressed in μg m^{-3}.

simulations with targeted emission reductions scenarios and the goal is to increase its resolution for a better representation of the local scale. Definitively, our approach paves the way for producing fast scenario simulations at high resolution to feed this type of models, but care must be taken to ensure that a minimum of physics is embedded to deal with non-linearities as previously mentioned. For instance, the case of Ozone but also the formation of secondary particles like the ammonium nitrate can be highlighted. Our approach could also inspire new developments in SHERPA-like models benefiting from more recent developments in machine learning techniques on image processing and analyses. Moreover, our developments can be easily adapted to any other CTM outputs.

5. Conclusion

In this paper, we developed and evaluated the relevance of the neural-network super-resolution approaches to downscale coarse CTM simulations focusing on three regulatory pollutants: NO_2, $PM_{2.5}$ and PM_{10}. These learning-based techniques take advantage of fast coarse simulation outputs from CTM embedding complex mathematical representations of physics and chemistry and particularly the long-range transport of pollutants, with local features which can be retrieved by NN approaches. The reported quantitative and qualitative evaluation for both simulation and real observation datasets support the relevance of the neural-network-based downscaling for the operational monitoring and forecasting of air quality.

Future works may focus on how to integrate physical constraints in the neural network to improve these first encouraging results on a very complex area with steep slopes enhancing local effects. It is especially relevant for O_3, in [17], a special treatment for such a secondary pollutant is proposed based on the two main equations of the ozone chemistry involving NOx and Ozone. If the correlations for NO_2 are even better for the RCAN architecture compared to CHIMERE *versus* observations, the discrepancies in terms of bias can be a consequence of the local interactions with Ozone that are not considered in our methodology. This type of physical processes can be easily implemented in an efficient NN-based scheme as a way of forcing the consistency between the super resolution outputs for NO_2, NO and O_3. This directly relates to one of the main branch of physically-guided neural networks that aims at designing specific NN architectures to embed the physics in the modeling system. An other option would be to keep similar CNN and attention-based architectures proposed in the paper while adding additional constraints on the physics in the loss function: it is an active field of research in what is called physically-informed neural networks [39, 40].

At last, let us remind that using neural network is complementary of developing more and more complex physical models. They are good instruments to simplify complex models for operational uses (by catching the main patterns) and offering the possibility to develop more and more sophisticated deterministic models representing the "real world".

Acknowledgments

This research was funded by the DGA (French Directorate General of Armaments; grant no. 2018 60 0074) in the framework of the NETDESA project. It was also supported by ANR Projects OceaniX. It benefited from HPC and GPU resources from Azure (Microsoft EU Ocean awards) and from GENCI-IDRIS (Grant 2020-101030).

References

[1] UN. World Urbanization Prospects: The 2018 Revision. Technical Report ST/ESA/SER.A/420, Department of Economic and Social Affairs, Population Division, United Nations, New York, USA, 2019.

[2] EEA. *Air quality in Europe: 2019 report*. Publications Office, LU, 2019.

[3] S. Mailler, L. Menut, D. Khvorostyanov, M. Valari, F. Couvidat, G. Siour, S. Turquety, R. Briant, P. Tuccella, B. Bessagnet, A. Colette, L. Létinois, K. Markakis, and F. Meleux. Chimere-2017: from urban to hemispheric chemistry-transport modeling. *Geoscientific Model Development*, 10(6):2397–2423, 2017.

[4] V. Marécal, V.-H. Peuch, C. Andersson, S. Andersson, J. Arteta, M. Beekmann, A. Benedictow, R. Bergstrm, B. Bessagnet, A. Cansado, F. Chéroux, A. Colette, A. Coman, R.L. Curier, H.A.C.D. Van Der Gon, A. Drouin, H. Elbern, E. Emili, R.J. Engelen, H.J. Eskes, G. Foret, E. Friese, M. Gauss, C. Giannaros, J. Guth, M. Joly, E. Jaumouillé, B. Josse, N. Kadygrov, J.W. Kaiser, K. Krajsek, J. Kuenen, U. Kumar, N. Liora, E. Lopez, L. Malherbe, I. Martinez, D. Melas, F. Meleux, L. Menut, P. Moinat, T. Morales, J. Parmentier, A. Piacentini, M. Plu, A. Poupkou, S. Queguiner, L. Robertson, L. Rouïl, M. Schaap, A. Segers, M. Sofiev, L. Tarasson, M. Thomas, R. Timmermans, Á. Valdebenito, P. Van Velthoven, R. Van Versendaal, J. Vira, and A. Ung. A regional air quality forecasting system over Europe: The MACC-II daily ensemble production. *Geoscientific Model Development*, 8(9):2777–2813, 2015.

[5] L. Rouïl, C. Honoré, R. Vautard, M. Beekmann, B. Bessagnet, L. Malherbe, F. Meleux, A. Dufour, C. Elichegaray, J.M. Flaud, L. Menut, D. Martin, A. Peuch, V.H. Peuch, and N. Poisson. PREV'AIR : an operational forecasting and mapping system for air quality in Europe. *BAMS*, 90:73–83, 2009.

[6] Sabine Host, Cécile Honoré, Fabrice Joly, Adrien Saunal, Alain Le Tertre, and Sylvia Medina. Implementation of various hypothetical low emission zone scenarios in Greater Paris: Assessment of fine-scale reduction in exposure and expected health benefits. *Environmental Research*, 185:109405, 2020.

[7] Kıymet Kaya and Şule Gündüz Öüğüdücü. Deep Flexible Sequential (DFS) Model for Air Pollution Forecasting. *Scientific Reports*, 10(1):3346, December 2020.

[8] Tianyu Liu, Yongzhi Ying, Yanyan Xu, Dengfeng Ke, and Kaile Su. Fine-Grained Air Quality Prediction using Attention Based Neural Network. In *2018 International Joint Conference on Neural Networks (IJCNN)*, pages 1–6, Rio de Janeiro, July 2018. IEEE.

[9] Seyedeh Reyhaneh Shams, Ali Jahani, Saba Kalantary, Mazaher Moeinaddini, and Nematollah Khorasani. Artificial intelligence accuracy assessment in NO2 concentration forecasting of metropolises air. *Scientific Reports*, 11(1):1805, December 2021.

[10] Ditsuhi Iskandaryan, Francisco Ramos, and Sergio Trilles. Air Quality Prediction in Smart Cities Using Machine Learning Technologies based on Sensor Data: A Review. *Applied Sciences*, 10(7):2401, April 2020.

[11] Hamza Turabieh, Alaa Sheta, Malik Braik, and Elvira Kovač-Andrić. A Layered Recurrent Neural Network for Imputing Air Pollutants Missing Data and Prediction of NO_2, O_3, PM_{10}, and $PM_{2.5}$. In Abdo Abou Jaoude, editor, *Forecasting in Mathematics - Recent Advances, New Perspectives and Applications*. IntechOpen, January 2021.

[12] Sheen Mclean Cabaneros, John Kaiser Calautit, and Ben Richard Hughes. A review of artificial neural network models for ambient air pollution prediction. *Environmental Modelling & Software*, 119:285–304, September 2019.

[13] Ichrak Mokhtari, Walid Bechkit, Herve Rivano, and Mouloud Riadh Yaici. Uncertainty-Aware Deep Learning Architectures for Highly Dynamic Air Quality Prediction. *IEEE Access*, 9:14765–14778, 2021.

[14] Yann LeCun, Yoshua Bengio, and Geoffrey Hinton. Deep learning. *Nature*, 521(7553):436–444, May 2015.

[15] Andrey Vlasenko, Volker Matthias, and Ulrich Callies. Simulation of Chemical Transport Model Estimates by means of Neural Network using Meteorological Data. *Atmospheric Environment*, page 118236, January 2021.

[16] Komal Shukla, Nikhil Dadheech, Prashant Kumar, and Mukesh Khare. Regression-based flexible models for photochemical air pollutants in the national capital territory of megacity Delhi. *Chemosphere*, 272:129611, June 2021.

[17] B. Bessagnet, F. Couvidat, and V. Lemaire. A statistical physics approach to perform fast highly-resolved air quality simulations ? A new step towards the meta-modelling of chemistry transport models. *Environmental Modelling and Software*, 116:100–109, 2019.

[18] Markus Amann, Imrich Bertok, Jens Borken-Kleefeld, Janusz Cofala, Chris Heyes, Lena Hglund-Isaksson, Zbigniew Klimont, Binh Nguyen, Maximilian Posch, Peter Rafaj, Robert Sandler, Wolfgang Schpp, Fabian Wagner, and Wilfried Winiwarter. Cost-effective control of air quality and greenhouse gases in europe: Modeling and policy applications. *Environmental Modelling & Software*, 26(12):1489–1501, 2011.

[19] Markus Amann, Janusz Cofala, Artur Gzella, Chris Heyes, Zbigniew Klimont, and Wolfgang Schpp. Estimating concentrations of fine particulate matter in urban background air of european cities. Technical Report Interim Report IR-07-001, IIASA, 2007.

[20] R. Briant, P. Tuccella, A. Deroubaix, D. Khvorostyanov, L. Menut, S. Mailler, and S. Turquety. Aerosol–radiation interaction modelling using online coupling between the wrf 3.7.1 meteorological model and the chimere 2016 chemistry-transport model, through the oasis3-mct coupler. *Geoscientific Model Development*, 10(2):927–944, 2017.

[21] Paolo Tuccella, Laurent Menut, Rgis Briant, Adrien Deroubaix, Dmitry Khvorostyanov, Sylvain Mailler, Guillaume Siour, and Solne Turquety. Implementation of aerosol-cloud interaction within wrf-chimere online coupled model: Evaluation and investigation of the indirect radiative effect from anthropogenic emission reduction on the benelux union. *Atmosphere*, 10(1), 2019.

[22] F. Couvidat, B. Bessagnet, M. Garcia-Vivanco, E. Real, L. Menut, and A. Colette. Development of an inorganic and organic aerosol model (chimere 2017β v1.0): seasonal and spatial evaluation over europe. *Geoscientific Model Development*, 11(1):165–194, 2018.

[23] A. B. Guenther, X. Jiang, C. L. Heald, T. Sakulyanontvittaya, T. Duhl, L. K. Emmons, and X. Wang. The model of emissions of gases and aerosols from nature version 2.1 (megan2.1): an extended and updated framework for modeling biogenic emissions. *Geoscientific Model Development*, 5(6):1471–1492, 2012.

[24] NCAR/UCAR. Ncep fnl operational model global tropospheric analyses, continuing from july 1999, research data archive at the national center for atmospheric research, computational and information systems laboratory, 2000. https://doi.org/10.5065/D6M043C6.

[25] B. Bessagnet, L. Menut, R. Lapere, F. Couvidat, J.-L. Jaffrezo, S. Mailler, O. Favez, R. Pennel, and G. Siour. High resolution chemistry transport modeling with the on-line CHIMERE-WRF model over the French Alps-Analysis of a feedback of surface particulate matter concentrations on mountain meteorology. *Atmosphere*, 11(6), 2020.

[26] Maxime Beauchamp, Ronan Fablet, Clément Ubelmann, Maxime Ballarotta, and Bertrand Chapron. Intercomparison of data-driven and learning-based interpolations of along-track nadir and wide-swath swot altimetry observations. *Remote Sensing*, 12(22), 2020.

[27] Yulun Zhang, Kunpeng Li, Kai Li, Lichen Wang, Bineng Zhong, and Yun Fu. Image super-

resolution using very deep residual channel attention networks, 2018.

[28] Dzmitry Bahdanau, Kyunghyun Cho, and Yoshua Bengio. Neural machine translation by jointly learning to align and translate, 2016.

[29] Minh-Thang Luong, Hieu Pham, and Christopher D. Manning. Effective approaches to attention-based neural machine translation, 2015.

[30] Redouane Lguensat, Phi Huynh Viet, Miao Sun, Ge Chen, Tian Fenglin, Bertrand Chapron, and Ronan Fablet. Data-driven interpolation of sea level anomalies using analog data assimilation. *Remote Sensing*, 11(7), 2019.

[31] S. Ouala, R. Fablet, C. Herzet, B. Chapron, A Pascual, F. Collard, and L. Gaultier. Neural Network Based Kalman Filters for the Spatio-Temporal Interpolation of Satellite-Derived Sea Surface Temperature. *Remote Sensing*, 10(12):1864, 2018.

[32] Julien Brajard, Alberto Carrassi, Marc Bocquet, and Laurent Bertino. Combining data assimilation and machine learning to infer unresolved scale parametrization, 2021.

[33] Ronan Fablet, Lucas Drumetz, and Francois Rousseau. Joint learning of variational representations and solvers for inverse problems with partially-observed data. *arXiv:2006.03653 [physics]*, 2020. arXiv:2006.03653.

[34] A. Clappier, E. Pisoni, and P. Thunis. A new approach to design source-receptor relationships for air quality modelling. *Environmental Modelling & Software*, 74:66–74, 2015.

[35] E. Pisoni, A. Clappier, B. Degraeuwe, and P. Thunis. Adding spatial flexibility to source-receptor relationships for air quality modeling. *Environmental Modelling & Software*, 90:68–77, 2017.

[36] European Union. Ambient air quality and cleaner air for europe. *Directive 2008/50/EC of the European Parliament and of the Council of 21 May 2008 OJ L 152*, pages 1–44, 2008.

[37] Antonio Pez, Steven Farber, and David Wheeler. A simulation-based study of geographically weighted regression as a method for investigating spatially varying relationships. *Environment and Planning A: Economy and Space*, 43(12):2992–3010, 2011.

[38] Christopher Lloyd. *Local Models for Spatial Analysis, Second Edition.* Taylor and Francis, 2011.

[39] Maziar Raissi. Deep hidden physics models: Deep learning of nonlinear partial differential equations. *Journal of Machine Learning Research*, 19(25):1–24, 2018.

[40] Ameya D. Jagtap and George Em Karniadakis. Extended physics-informed neural networks (xpinns): A generalized space-time domain decomposition based deep learning framework for nonlinear partial differential equations. *Communications in Computational Physics*, 28(5):2002–2041, 2020.

Appendices

A. Error statistics and performances for PM_{10}

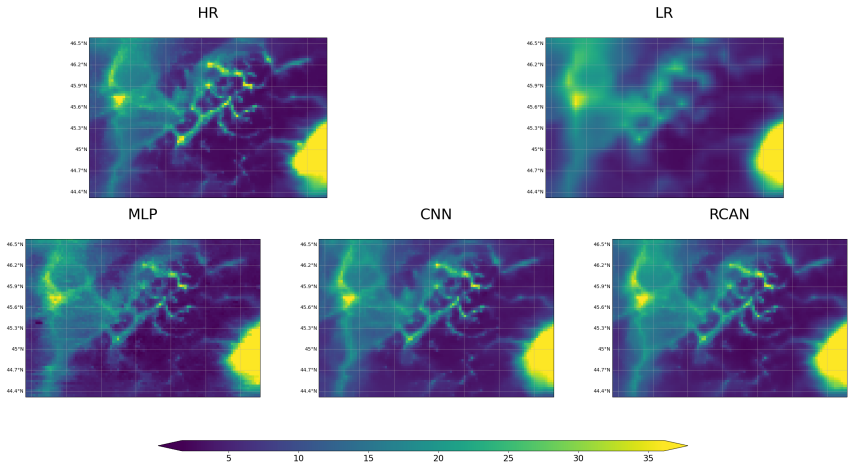

Figure A.1: PM_{10} mean concentrations over the validation period for CHIMERE high-resolution and coarse resolution (top line) and three NN-based super resolution architectures (bottom line): from left to right, pixel-based independent multi-layer perceptron (MLP), Convolutional neural network (CNN) and Residual channel attention network (RCAN)

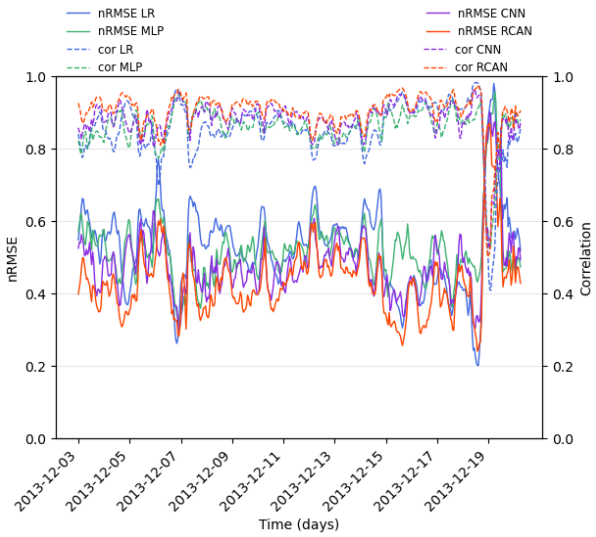

Figure A.2: PM_{10} nRMSE and correlation time series (a) of coarse resolution, pixel-based independent multi-layer perceptron (MLP), Convolutional neural network (CNN) and Residual channel attention network (RCAN) and summary statistics over the validation period as Taylor diagrams (b)

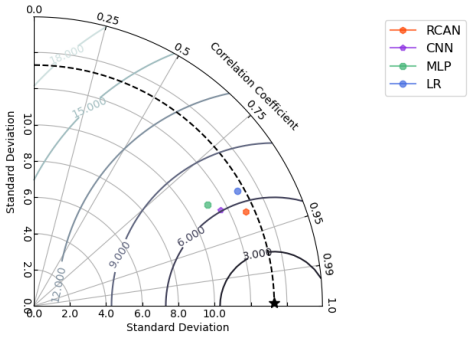

Figure A.3: PM_{10} summary statistics over the validation period as Taylor diagrams for low resolution simulation (LR), multi-layer perceptron (MLP), Convolutional neural network (CNN) and Residual channel attention network (RCAN) versus the high resolution (HR) considered as the "truth".

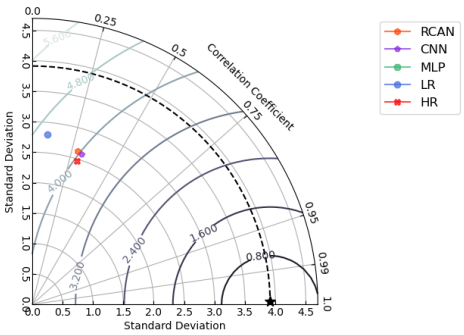

(a) All rural

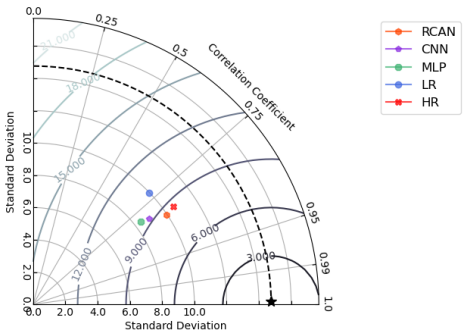

(b) All urban

Species	Method	Typology	# stations	Obs.	Mod.	Bias	RMSE	Cor.
PM_{10}	HR	RUR	4	11.24	8.15	-3.09	5.01	0.30
	LR				7.66	-3.58	5.83	0.09
	MLP				4.93	-6.31	8.78	-0.24
	CNN				8.18	-3.06	5.01	0.31
	RCAN				8.31	-2.93	4.99	0.28
	HR	URB	35	43.75	23.52	-20.23	21.97	0.82
	LR				20.13	-23.62	25.75	0.72
	MLP				20.59	-23.15	25.05	0.79
	CNN				22.25	,-21.50	23.40	0.80
	RCAN				23.00	-20.75	22.49	0.83

(c) Daily statistics

Figure A.4: PM_{10} daily statistics of high resolution (HR), coarse resolution (LR), pixel-based independent multi-layer perceptron (MLP), Convolutional neural network (CNN) and Residual channel attention network (RCAN) for comparison with all rural observations (a) and all urban observations (b) as Taylor diagrams summarized in table (c). Observations, model outputs, biases and RMSE are expressed in μg m^{-3}.

B. Comparison with the hourly observations

Species	Method	Typology	# stations	Obs.	Mod.	Bias	RMSE	Cor.
NO_2	HR	RUR	7	13.64	4.71	-8.92	11.12	0.35
	LR				5.54	-8.09	10.82	0.16
	MLP				4.54	-9.09	11.45	0.20
	CNN				5.04	-8.59	10.88	0.33
	RCAN				4.93	-8.70	11.07	0.25
	HR	URB	40	48.67	33.62	-15.05	19.67	0.65
	LR				24.60	-24.06	26.90	0.61
	MLP				30.27	-18.39	21.40	,0.69
	CNN				32.24	,-16.42	20.07	0.69
	RCAN				28.31	-20.36	23.23	0.68

Table B.1: NO_2 hourly statistics of high resolution (HR), coarse resolution (LR), pixel-based independent multi-layer perceptron (MLP), Convolutional neural network (CNN) and Residual channel attention network (RCAN). Observations, model outputs, biases and RMSE are expressed in μg m^{-3}.

Species	Method	Typology	# stations	Obs.	Mod.	Bias	RMSE	Cor.
$PM_{2.5}$	HR	RUR	3	13.20	7.95	-4.83	8.16	0.30
	LR				6.35	-6.58	8.97	0.42
	MLP				6.54	-6.52	8.86	0.46
	CNN				6.85	-5.95	8.48	0.43
	RCAN				7.91	-4.88	7.71	0.45
	HR	URB	12	36.65	24.84	-11.81	15.00	0.80
	LR				21.71	-14.94	18.44	0.71
	MLP				21.41	-15.23	18.31	0.76
	CNN				21.70	,-14.94	17.83	0.78
	RCAN				25.96	-10.69	14.23	0.79

Table B.2: $PM_{2.5}$ hourly statistics of high resolution (HR), coarse resolution (LR), pixel-based independent multi-layer perceptron (MLP), Convolutional neural network (CNN) and Residual channel attention network (RCAN). Observations, model outputs, biases and RMSE are expressed in μg m^{-3}.

Species	Method	Typology	# stations	Obs.	Mod.	Bias	RMSE	Cor.
PM_{10}	HR	RUR	4	11.44	8.24	-3.20	6.24	0.25
	LR				7.73	-3.71	6.75	0.18
	MLP				4.84	-6.59	9.82	-0.12
	CNN				8.30	-3.14	6.18	0.27
	RCAN				8.42	-3.01	6.05	0.28
	HR	URB	35	44.87	23.95	-20.92	23.38	0.77
	LR				20.41	-24.45	27.29	0.68
	MLP				20.91	-23.96	26.60	0.73
	CNN				22.51	,-22.36	24.93	0.76
	RCAN				23.41	-21.46	23.92	0.78

Table B.3: PM_{10} hourly statistics of high resolution (HR), coarse resolution (LR), pixel-based independent multi-layer perceptron (MLP), Convolutional neural network (CNN) and Residual channel attention network (RCAN). Observations, model outputs, biases and RMSE are expressed in μg m^{-3}.

C. Statistics on Δ

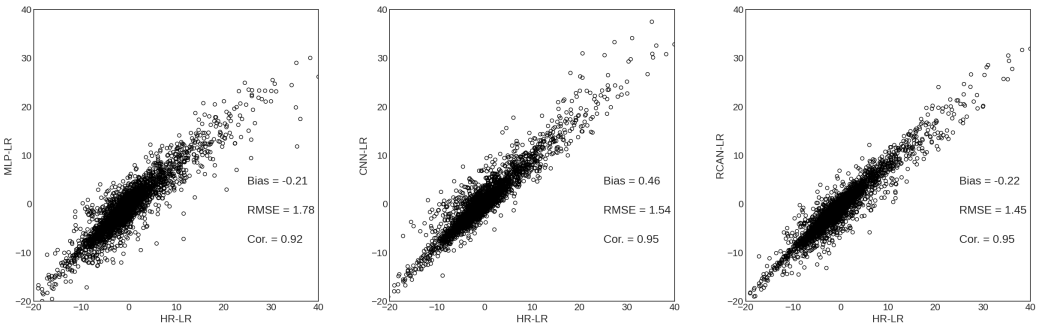

(a) NO_2

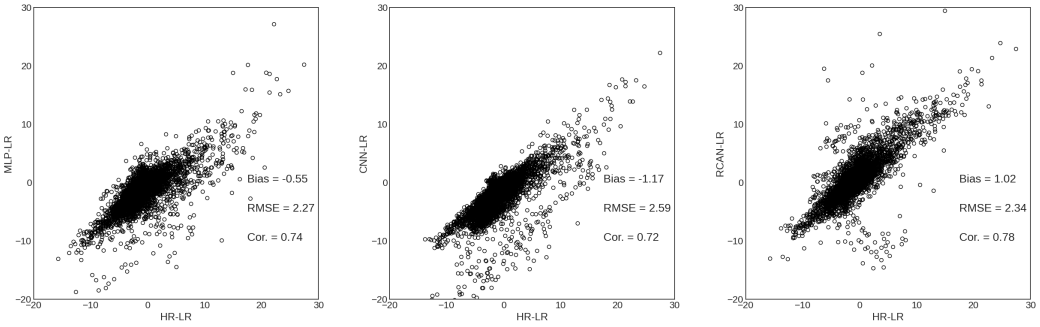

(b) $PM_{2.5}$

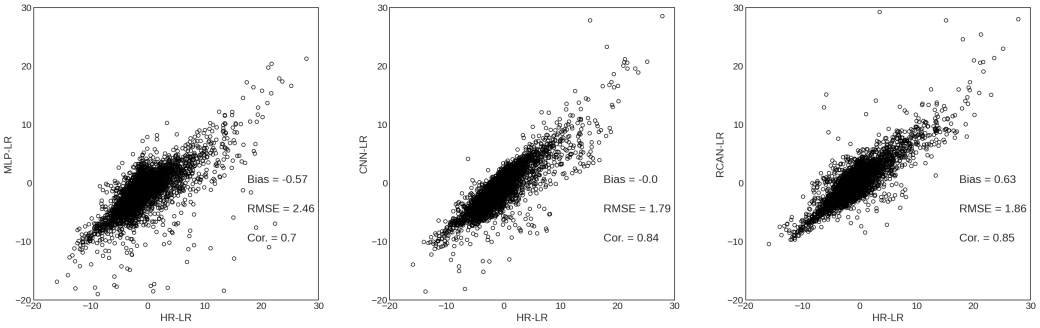

(c) PM_{10}

Figure C.5: Scatterplots between the "true" increment HR-LR and the SR-based increments: from left to right, MLP-LR, CNN-LR and RCAN-LR for NO_2 (a), $PM_{2.5}$ (b) and PM_{10} (c) expressed in μg m^{-3}.

D. Definition of error statistics

The mean bias (MB), Pearson correlation (R), the root mean square error (RMSE) and its "normalized" version (nRMSE) are defined herebelow for n the number of data, M the model predicted value and O the corresponding observation or HR "truth". $\overline{O}$ denotes the mean value of the HR truth along the validation period.

$$\bar{V} = \frac{1}{n}\sum_{i=1}^{n} V_i \quad V = O, M \tag{6}$$

$$MB = \frac{1}{n}\sum_{i=1}^{n} (M_i - O_i) \tag{7}$$

$$RMSE = \sqrt{\frac{1}{n}\sum_{i=1}^{n}(M_i - O_i)^2} \tag{8}$$

$$nRMSE = \frac{\sqrt{\sum_{i=1}^{n}(M_i - O_i)^2}}{\sqrt{\sum_{i=1}^{n}(O_i - \bar{O})^2}} \tag{9}$$

$$R = \frac{\sum_{i=1}^{n}(M_i - \bar{M})(O_i - \bar{O})}{\sqrt{\sum_{i=1}^{n}(M_i - \bar{M})^2}\sqrt{\sum_{i=1}^{n}(O_i - \bar{O})^2}} \tag{10}$$